OPEN ACCESS
IOP Publishing | ISECAEP
Journal of Reliability Science and Engineering
J. Reliab. Sci. Eng. **2** (2026) 045401 (14pp)
https://doi.org/10.1088/3050-2454/aea09c

Performance dispersion analysis of integrated internal-external ballistics for solid divert control motors under multi-source uncertainty

Li Shuaiwei, Wu Zeping*, Jia Junkai, Tian Lei, Wang Tianci and Zhang Jie

College of Aerospace Science and Engineering, National University of Defense Technology, Changsha 410073, People's Republic of China

E-mail: zeping123@nudt.edu.cn

Received 23 June 2026, revised 28 July 2026
Accepted for publication 28 August 2026
Published 11 September 2026

Abstract

Uncertainties arising from control deviations, geometric deviations, and propellant property deviations during the design, manufacturing, and operation of solid divert control motors (SDCMs) cause the thrust output to deviate from its nominal value, thereby affecting the strike accuracy of kinetic interceptors. To quantitatively evaluate the influence of these uncertainties on strike accuracy, an integrated internal-external ballistic dynamic model of the SDCM is established. Based on this model, a performance dispersion analysis method for the integrated internal-external ballistics is proposed using polynomial chaos expansions. The effects of control deviations, geometric deviations, and propellant property uncertainties on the miss distance are systematically analyzed, and Sobol' sensitivity analysis is performed to quantify the contribution of each uncertain parameter to the variability of the miss distance. The quantitative evaluation of uncertainty effects provides valuable guidance for the optimal design of SDCMs.

Keywords: solid divert control motor, strike accuracy, polynomial chaos expansion, dispersion analysis, uncertainty quantification, Sobol' sensitivity analysis

1. Introduction

The solid divert control motor (SDCM) is capable of adjusting its operating state on demand according to the control requirements of a kinetic interceptor, thereby generating the required thrust, and offers advantages such as structural simplicity and high reliability [1–3]. During the thrust regulation process, the SDCM is subject to the coupled effects of multiple uncertainty sources, including control system deviations, geometric dimensional deviations, and propellant material property uncertainties. These uncertainties lead to deviations of the thrust performance from its nominal value, directly affecting the maneuverability of the kinetic interceptor and its strike accuracy against the target [4, 5]. Therefore, investigating the influence of multi-source uncertainties on the strike accuracy of kinetic interceptors is significant for improving overall system performance and reliability [6].

At present, research on the integrated internal-external ballistics of solid rocket motors remains limited, with existing studies primarily focusing on design optimization and performance prediction [7]. Lei *et al* [8] proposed an integrated design method for solid rocket internal-external ballistics. By establishing a coupled model of nozzle ablation and propellant burn rate that accounts for the influence of flight overload,

* Author to whom any correspondence should be addressed.

Original content from this work may be used under the terms of the Creative Commons Attribution 4.0 licence. Any further distribution of this work must maintain attribution to the author(s) and the title of the work, journal citation and DOI.

© 2026 The Author(s). Published by IOP Publishing Ltd on behalf of the Institute of Systems Engineering, China Academy of Engineering Physics

the integrated design and refined performance prediction were achieved. Wu *et al* [9] developed an integrated optimization approach that couples engine performance with ballistic simulation, which significantly improves the low-altitude supersonic cruise time of the target missile under constraints of structural configuration, layout, and stability. Su *et al* [10] explored the integrated optimization of vehicle-level and propulsion-system design for a typical solid launch vehicle. By employing multiple optimization approaches for the first-stage motor, the payload capability of the launch vehicle was significantly improved. However, the aforementioned studies on integrated internal-external ballistics are primarily deterministic, focusing on performance evaluation and design optimization. The influence of uncertainties within the coupled internal-external ballistic system has not been sufficiently considered, making it difficult to capture the performance dispersion characteristics during the engine operating process.

In recent years, extensive studies have been conducted by researchers worldwide on the uncertainty analysis of solid rocket motor performance [11]. Gao *et al* [12] employed Monte Carlo Simulation (MCS) to investigate the influence of geometric parameter uncertainties on the thrust performance of pintle-type solid attitude and divert control motors under varying operating conditions, and quantitatively evaluated uncertainties in the real-time thrust regulation process. However, MCS requires substantial data and is computationally expensive, limiting its applicability to uncertainty-based design of SDCMs. To address this issue, surrogate modeling techniques have been introduced to improve the efficiency of uncertainty analysis. Zhu *et al* [13] proposed a hybrid uncertainty optimization method integrating polynomial chaos expansions (PCE) with interval analysis, which effectively resolves the quantification of mixed stochastic and interval uncertainties in solid and liquid rocket engine design. Xiao *et al* [14] incorporated evidence theory to handle epistemic uncertainties in parameter design of solid and liquid rocket engines, and combined it with a PCE model to enhance computational efficiency in uncertainty quantification. Shi *et al* [15] developed a high-accuracy surrogate modeling approach that integrates Proper Orthogonal Decomposition, the Kriging model, and the Maximum Entropy Method, enabling efficient prediction of the uncertainty distribution of solid rocket motor thrust curves while significantly reducing computational time with a confidence level of 98%. Balesdent *et al* [16] proposed a method combining multidisciplinary design optimization with pseudo-spectral optimal control for uncertainty quantification in launch vehicle design, significantly improving the computational efficiency of global sensitivity analysis.

Although extensive research has been conducted on the thrust performance analysis of solid rocket motors and integrated internal-external dynamic ballistic modeling, leading to significant advances in propulsion performance prediction and ballistic characterization, existing studies have primarily focused on propulsion performance analysis or deterministic modeling of the internal-external ballistic process. However, a systematic framework for characterizing the propagation of multiple uncertainty sources in the coupled internal-external ballistic system of SDCMs has yet to be established. In particular, no systematic framework exists for modeling how multiple uncertainty sources propagate through the coupled internal-external ballistic process. Quantitative analysis of how these sources ultimately affect the miss distance is also lacking. Therefore, further investigation of the performance dispersion characteristics of integrated internal-external ballistics of SDCMs under multi-source uncertainties is required to provide theoretical support and design guidance for improving the strike accuracy of kinetic interceptors.

Based on the above research background, this paper investigates the performance dispersion characteristics of the integrated internal-external ballistics of solid divert control motors under multi-source uncertainties. First, an integrated internal-external ballistic dynamic model of the SDCM is established. Next, MCS is performed by considering multiple uncertainty sources, including control deviations, geometric deviations, and propellant property deviations. Subsequently, a total of 3500 sample points are generated over the entire input space using optimized Latin hypercube sampling (OLHS) to construct the PCE surrogate model, and the local and global predictive accuracy of the surrogate model is verified. The PCE surrogate model is used to analyze the uncertainty-induced dispersion of miss distance. Finally, Sobol' sensitivity analysis is performed to quantify the contribution of different uncertainty sources to the variability of the miss distance, and the uncertain parameters are ranked according to their importance.

The remainder of this paper is organized as follows. Section 2 introduces the integrated internal-external ballistic dynamic modeling framework of the SDCM, including the internal ballistic model, external ballistic model, proportional navigation guidance law, and the integrated dynamic model. Section 3 presents the performance dispersion analysis of the integrated internal-external ballistics under multi-source uncertainties. A PCE surrogate model is constructed and validated, followed by uncertainty quantification and importance ranking of the influencing factors. Finally, section 4 concludes the paper and summarizes the main findings.

2. Integrated modeling of internal-external ballistics dynamic for SDCMs

2.1. Internal ballistic model of SDCMs

The pintle-type SDCM investigated in this study employs four divert nozzles that share a common combustion chamber. Figure 1 shows the configuration of the SDCM installed on the kinetic interceptor. The motor is mounted at the center of mass of the kinetic interceptor, and the nozzles are arranged in an axisymmetric configuration. During operation, the motor provides the lateral divert force required for the interceptor's transverse maneuvering [17]. The four divert nozzles are labeled D1, D2, D3, and D4 in a clockwise direction.

The thrust calculation formula for a single valve of the SDCM can be derived based on the conservation of momentum or the pressure distribution on the internal and external

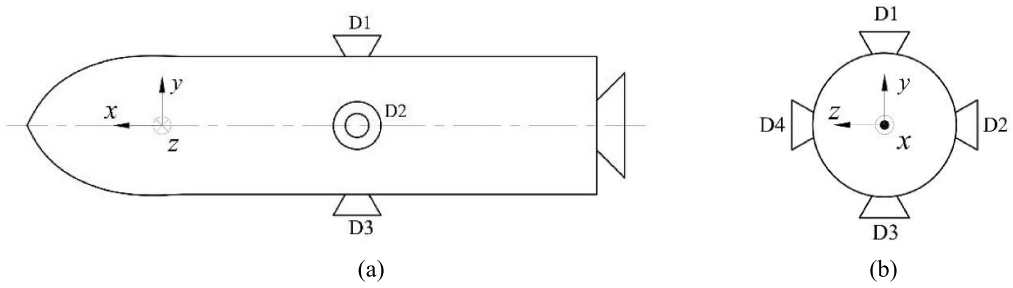


Figure 1. (a) Overall schematic diagram of kinetic interceptor and (b) SDCM configuration.

surfaces of the motor, and is given as [18, 19]

$$F_i = C_{\mathrm{F}i} p_{\mathrm{c}} A_{\mathrm{t}i} \tag{1}$$

where $C_{\mathrm{F}i}$ denotes the thrust coefficient of the ith valve, $i = 1,2,3,4$ represent the indices of the four valves, p_{c} is the combustion chamber pressure of the motor, and $A_{\mathrm{t}i}$ is the equivalent throat area of the ith valve.

The equivalent throat area of the nozzle refers to the minimum flow passage area after the insertion of the pintle. According to equation (1), the equivalent throat area is a key factor affecting the output thrust of the divert control motor [20]. In this study, the method reported in [21] is employed to calculate the equivalent throat area of the nozzle.

The SDCM considered in this paper adopts an end-burning propellant configuration with a constant burning surface. Accordingly, the zero-dimensional internal ballistic governing equations can be expressed as follows [22]

$$\frac{V_{\mathrm{c}}}{\Gamma^2 c^{*2}} \frac{\mathrm{d}p_{\mathrm{c}}}{\mathrm{d}t} = \rho_{\mathrm{p}} A_{\mathrm{b}} a p_{\mathrm{c}}^{n} - \frac{p_{\mathrm{c}} A_{\mathrm{tt}}}{c^*} \tag{2}$$

where c^* denotes the characteristic velocity of the propellant, ρ_{p} is the propellant density, A_{b} represents the burning surface area of the propellant, a is the burn rate coefficient, and n is the pressure exponent of the propellant. V_{c} denotes the free volume of the combustion chamber, A_{tt} is the total throat area of the four valves, and Γ is a function of the specific heat ratio k, which is expressed as follows

$$\Gamma = \sqrt{k}\left(\frac{2}{k+1}\right)^{\frac{k+1}{2(k-1)}}. \tag{3}$$

To ensure stable thrust output, the SDCM is typically required to satisfy the combustion chamber pressure equilibrium constraint during operation. The total throat area A_{tt} is regulated by adjusting the opening of the four valves; therefore, the pressure equilibrium constraint can be equivalently transformed into a constraint on the total opening of the four divert nozzles during coordinated operation. For the end-burning propellant with a constant burning surface, when the combustion chamber pressure reaches equilibrium, $\mathrm{d}p_{\mathrm{c}}/\mathrm{d}t = 0$, and the steady-state chamber pressure can be expressed as follows [23]

$$p_{\mathrm{c,eq}} = \left(\rho_{\mathrm{p}} c^* a \frac{A_{\mathrm{b}}}{A_{\mathrm{tt}}}\right)^{\frac{1}{1-n}}. \tag{4}$$

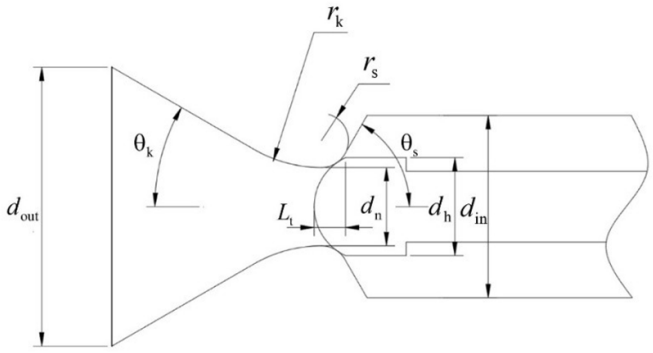


Figure 2. Solid divert control motor nozzle configuration.

The equilibrium combustion chamber pressure $p_{\mathrm{c,eq}}$ is taken as the operating pressure of the SDCM investigated in this study. Figure 2 illustrates the configuration of a single nozzle of the SDCM. Table 1 lists the corresponding parameters. The parameter r denotes the propellant burning rate measured at a chamber pressure of 7 MPa, which is calculated according to the burning-rate law $r = ap^n$.

Assume that, at a certain instant during engine operation, the pintles of the four divert control valves are positioned at different locations. Figure 3 shows the force distribution acting on the engine.

The SDCM consists of a longitudinal channel and a lateral channel. The control forces generated in each channel can be expressed as

$$\begin{cases} Y_{1c} = F_3 - F_1 \\ Z_{1c} = F_4 - F_2 \end{cases}. \tag{5}$$

In this study, the total valve opening A_{tt} of the SDCM is assumed to be equal to the maximum opening of a single valve. The allocation of valve openings should prioritize the channel with the higher thrust demand, and only one valve in the high-thrust-demand channel is allowed to operate at a time. When $|\bar{Y}_{1c}| > |\bar{Z}_{1c}|$, the longitudinal channel is identified as the high-thrust-demand channel. In this case, if $\bar{Y}_{1c} > 0$, valve 3 operates while valve 1 remains fully closed, subject to the constraint

$$\begin{cases} -F_{\mathrm{dmax}} \leqslant \bar{Y}_{1c} \leqslant F_{\mathrm{dmax}} \\ -F_{\mathrm{dmax}} \leqslant \bar{Z}_{1c} \leqslant F_{\mathrm{dmax}} \end{cases} \tag{6}$$

Table 1. Solid divert control motor parameters table.

Parameters		Values
Configuration parameters of the motor	Nozzle exit diameter d_{out} /mm	45
	Nozzle expansion half-angle $\theta_k/\circ$	30
	Transition arc radius of expansion section r_k /mm	20
	Convergent section arc radius r_s /mm	4
	Nozzle convergent half-angle $\theta_s/\circ$	60
	Pintle head length L_t /mm	8
	Nozzle throat diameter d_n /mm	14
	Pintle diameter d_h /mm	16
	Nozzle inlet diameter d_{in} /mm	32
	Propellant burning surface radius r_b /mm	120
Propellant property parameters	Propellant density ρ_p / (kg m^{-3})	1700
	Burn rate r/(mm s^{-1})	15
	Characteristic velocity c^* /(m s^{-1})	1400
	Pressure exponent n	0.30

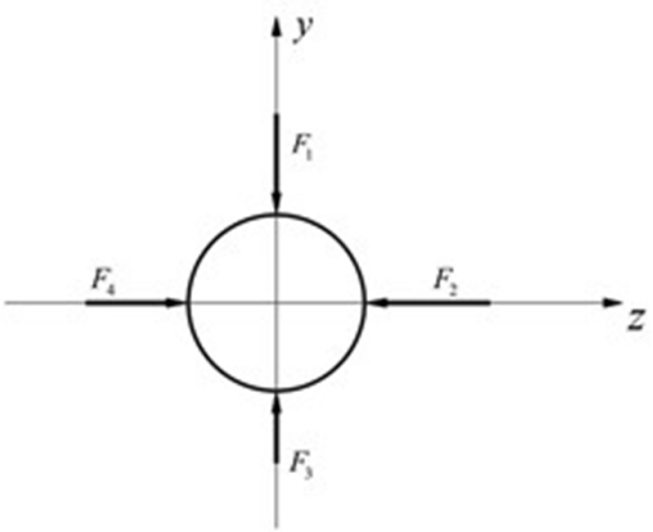


Figure 3. Schematic diagram of the force distribution acting on the solid divert control motor.

where $\bar{Y}_{1c}$ and $\bar{Z}_{1c}$ denote the desired control forces in the longitudinal and lateral channels, respectively, F_{dmax} denote the maximum thrust of a single divert control valve.

Taking the longitudinal channel as the high-thrust-demand channel as an example, the valve opening allocation strategy is described as follows. The required thrust provided by each valve in the longitudinal channel is given by

$$\begin{cases} F_1 = -\min(\bar{Y}_{1c}, 0) \\ F_3 = \max(\bar{Y}_{1c}, 0) \end{cases}. \tag{7}$$

Based on the required thrust in the longitudinal channel, the valve openings A_{t1} and A_{t3} can be determined. Given the total valve opening in the high-thrust-demand channel, the total opening constraint for the low-thrust-demand channel is expressed as

$$A_{tz} = A_{tt} - A_{t1} - A_{t3}. \tag{8}$$

If $A_{tz} = 0$, then $A_{t2} = A_{t4} = 0$. Otherwise, when $A_{tz} \neq 0$, the valve opening allocation problem in the lateral channel can be transformed into an optimization problem, which can be solved using the bisection method

$$\begin{cases} \text{thrust}(A_{tz} - A_{t2}) - \text{thrust}(A_{t2}) = \bar{Z}_{1c} \\ A_{t2d} = \max(A_{tz} - A_{tdmax}, 0) \\ A_{t2u} = \min(A_{tz}, A_{tdmax}) \\ A_{t2} \in [A_{t2d}, A_{t2u}] \end{cases} \tag{9}$$

where A_{tdmax} denotes the maximum opening of a single valve, and thrust(A_t) is a known function that maps the valve opening to the corresponding thrust. A_{t2d} and A_{t2u} denote the minimum and maximum valve openings, respectively, of a valve in the low-thrust-demand channel.

When $|\bar{Y}_{1c}| = |\bar{Z}_{1c}|$, the total valve opening is evenly distributed between the longitudinal and lateral channels.

$$A_{ty} = A_{tz} = \frac{A_{tt}}{2}. \tag{10}$$

In this case, the valve opening calculation procedures for the longitudinal and lateral channels are identical. Taking the lateral channel as an example, the valve opening allocation problem can be transformed into an optimization problem for solving the following system of equations.

$$\begin{cases} \text{thrust}(A_{tz} - A_{t2}) - \text{thrust}(A_{t2}) = \bar{Z}_{1c}. \\ A_{t2} \in [0, A_{tz}] \end{cases} \tag{11}$$

By employing this approach for valve opening allocation, an optimal set of valve openings for all four valves can be determined based on the desired divert thrusts in the longitudinal and lateral channels of the SDCM.

2.2. External ballistic model of the kinetic interceptor

The external ballistic equations of motion of the kinetic interceptor consist of the dynamic equations, kinematic equations, mass variation equation, and geometric relationship equations [24]. Since the terminal guidance phase of the

exo-atmospheric kinetic interceptor is relatively short and the relative engagement distance is limited, the effects associated with the Earth's rotation and Earth model simplifications are neglected [25]. Accordingly, the translational equations of motion of the kinetic interceptor, considering only gravitational force and the thrust generated by the SDCM, are established as follows

$$\begin{cases} m\frac{\mathrm{d}v_x}{\mathrm{d}t} = -Y_{1c}\sin\varphi + Z_{1c}\cos\varphi\sin\psi + m\frac{g'_r}{r}(x+R_{ox}) \\ m\frac{\mathrm{d}v_y}{\mathrm{d}t} = Y_{1c}\cos\varphi + Z_{1c}\sin\varphi\sin\psi + m\frac{g'_r}{r}(y+R_{oy}) \\ m\frac{\mathrm{d}v_z}{\mathrm{d}t} = Z_{1c}\cos\psi + m\frac{g'_r}{r}(z+R_{oz}) \end{cases} \tag{12}$$

where v_x, v_y, and v_z denote the velocity components of the kinetic interceptor along the three axes in the launch coordinate system; x, y, and z represent the position coordinates of the interceptor in the launch coordinate system; Y_{1c} and Z_{1c} are the normal and lateral control forces generated by the SDCM, respectively; m is the mass of the kinetic interceptor; g'_r denotes the gravitational acceleration toward the Earth's center; r is the distance from the interceptor's center of mass to the Earth's center; and R_{ox}, R_{oy}, and R_{oz} are the components of the geocentric radius vector of the launch point in the launch coordinate system.

In the launch coordinate system, the kinematic equations governing the motion of the kinetic interceptor's center of mass can be expressed as follows

$$\begin{cases} \frac{\mathrm{d}x}{\mathrm{d}t} = v_x \\ \frac{\mathrm{d}y}{\mathrm{d}t} = v_y \\ \frac{\mathrm{d}z}{\mathrm{d}t} = v_z \end{cases}. \tag{13}$$

The mass variation equation of the kinetic interceptor can be expressed as follows:

$$\frac{\mathrm{d}m}{\mathrm{d}t} = -ap_c^n A_b \rho_\mathrm{p}. \tag{14}$$

2.3. Proportional navigation guidance law

The line-of-sight angle and its rate for the kinetic interceptor are calculated as follows [26]

$$\begin{cases} q_\varepsilon = \arctan\left(\frac{y_\mathrm{r}}{\sqrt{x_\mathrm{r}^2+z_\mathrm{r}^2}}\right) \\ q_\beta = \arctan\left(\frac{-z_\mathrm{r}}{x_\mathrm{r}}\right) \\ \dot{q}_\varepsilon = \frac{(x_\mathrm{r}^2+z_\mathrm{r}^2)\dot{y}_\mathrm{r} - y_r(x_\mathrm{r}\dot{x}_\mathrm{r}+z_\mathrm{r}\dot{z}_\mathrm{r})}{(x_\mathrm{r}^2+y_r^2+z_\mathrm{r}^2)\sqrt{x_\mathrm{r}^2+z_\mathrm{r}^2}} \\ \dot{q}_\beta = \frac{z_r\dot{x}_\mathrm{r} - x_r\dot{z}_\mathrm{r}}{x_\mathrm{r}^2+z_\mathrm{r}^2} \end{cases} \tag{15}$$

where $x_\mathrm{r} = x_\mathrm{t} - x$, $y_\mathrm{r} = y_\mathrm{t} - y$ and $z_\mathrm{r} = z_\mathrm{t} - z$ denote the relative position components; $\dot{x}_\mathrm{r} = \dot{x}_\mathrm{t} - \dot{x}$, $\dot{y}_\mathrm{r} = \dot{y}_\mathrm{t} - \dot{y}$ and $\dot{z}_\mathrm{r} = \dot{z}_\mathrm{t} - \dot{z}$ represent the relative velocity components; x_t, y_t and z_t are the position coordinates of the target in the launch coordinate system.

The three-dimensional proportional navigation guidance law can be expressed as follows

$$\begin{cases} a_{\mathrm{my}_1} = N|\dot{R}|\dot{q}_\varepsilon \\ a_{\mathrm{mz}_1} = -N|\dot{R}_1|\dot{q}_\beta \end{cases} \tag{16}$$

where a_{my1} and a_{mz1} denote the guidance accelerations generated by the SDCM along the respective axes of the interceptor body coordinate system; N is the navigation constant; $|\dot{R}|$ and $|\dot{R}_1|$ represent the time derivatives of the relative distance between the target and the kinetic interceptor in the vertical and horizontal planes, respectively.

2.4. Integrated dynamic model of internal-external ballistics for the SDCM

Figure 4 illustrates the integrated internal-external ballistic dynamic model of the SDCM, which is established based on the aforementioned internal ballistic model, external ballistic model, and proportional navigation guidance law.

The terminal guidance module first obtains the guidance commands a_{my1} and a_{mz1}. The internal ballistic module responds to these commands by regulating the valve openings of the SDCM to achieve thrust allocation, thereby generating the divert control forces Y_{1c} and Z_{1c}. These forces are then taken as inputs to the external ballistic model. The external ballistic equations are numerically integrated using the fourth-order Runge–Kutta method to compute the relative distance between the kinetic interceptor and the target. When the relative distance reaches its minimum value, the numerical integration is terminated, and this minimum relative distance is defined as the miss distance R_m of the kinetic interceptor.

2.5. Numerical example

Table 2 lists the initial conditions of the kinetic interceptor and the motion parameters of the target.

Figure 5 shows the time histories of the control forces Y_{1c} and Z_{1c} generated in the longitudinal and lateral channels of the SDCM. Figure 6 illustrates the trajectories of the kinetic interceptor and the target.

The numerical simulation results indicate that the longitudinal channel of the SDCM consistently operates as the high-thrust demand channel. The kinetic interceptor achieves target interception at 17.72 s, with a final miss distance of 0.75 m.

3. Integrated performance dispersion analysis of internal-external ballistics for the SDCM

By comprehensively considering the effects of control deviations, geometric deviations, and propellant property uncertainties on strike accuracy, an uncertainty analysis of the integrated internal-external ballistics of the SDCM is conducted based on the established integrated model, employing PCE [27]. Table 3 lists the uncertain parameters considered in this study, and all parameters are assumed to follow normal distributions [21].

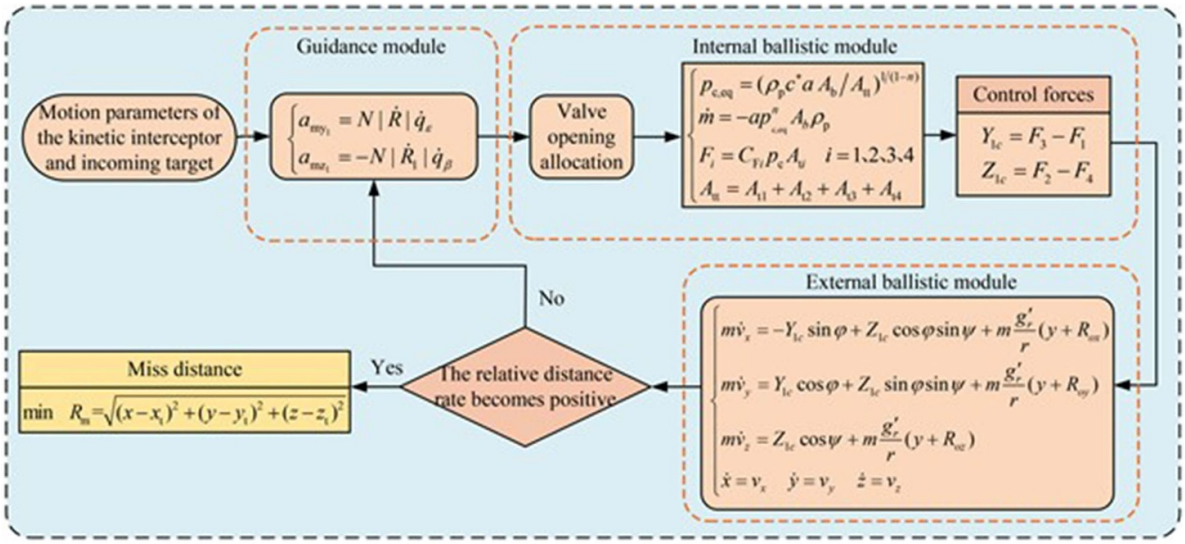


Figure 4. Integrated dynamic model of internal-external ballistics.

Table 2. Initial conditions of the kinetic interceptor and motion parameters of the target.

Initial kinematic parameters		Values
Initial conditions of the kinetic interceptor	Initial velocity (V_{xm}, V_{ym}, V_{zm}) /(km s^{-1})	(1.4,1.1,1.4)
	Initial position (x, y, z) /km	(0,70,0)
	Initial mass m /kg	80
Initial conditions of the target	Initial velocity (V_{xt}, V_{yt}, V_{zt}) /(km s^{-1})	(−0.6, −2, −2)
	Initial position (x_t, y_t, z_t) /km	(60 100,60)

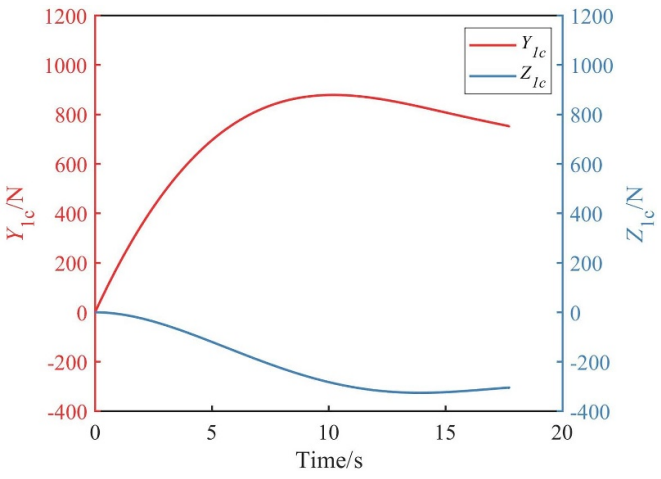


Figure 5. Variation curve of control force Y_{1c} and Z_{1c}.

A total of 60 000 samples are randomly generated using MCS, and figure 7 shows the dispersion of the kinetic interceptor miss distance.

Based on the 60 000 MCS simulation results, the miss distances of all samples remain below the threshold of 1.6 m indicated by the red line in figure 7. The overall dispersion of the miss distance is relatively small, with more scattered points distributed on the upper side than on the lower side, exhibiting a right-skewed distribution characteristic.

3.1. Construction of the PCE surrogate model

The PCE method can effectively characterize random variables with arbitrary probability distributions and theoretically exhibits exponential convergence properties, making it an efficient approach for uncertainty quantification analysis [28, 29].

As indicated in table 3, all input variables follow normal distributions. Therefore, Hermite orthogonal polynomials are employed to construct the PCE surrogate model. For an arbitrary random variable Y when the expansion is truncated at order p, the corresponding simplified PCE surrogate model can be expressed as follows

$$Y = \sum_{i=0}^{Q-1} c_i \Phi_i(\xi) \tag{17}$$

where c_i are the coefficients to be determined; $\Phi_i(\xi)$ denotes the pth order Hermite orthogonal polynomial of the d-dimensional uncertain variable ξ; and Q is the number of retained terms. The relationship between Q, the expansion order p, and the dimensionality d can be determined by equation (18)

$$Q = \frac{(d+p)!}{d!p!}. \tag{18}$$

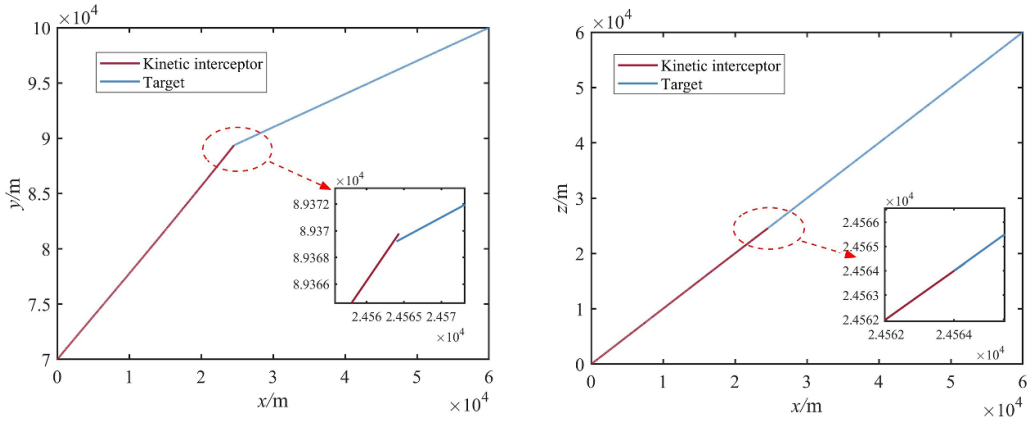


Figure 6. (a) Trajectories of the kinetic interceptor and the target projected onto the $x-y$ plane. (b) Trajectories of the kinetic interceptor and the target projected onto the $x-z$ plane.

Table 3. Uncertainty variables statistics.

Random variables		Mean value	Standard deviation
Control deviation	Pintle displacement Δx_{h}/mm	0	0.05
Geometric parameters	Pintle diameter d_{h}/mm	16	0.05
	Pintle head length L_{t}/mm	8	0.05
	Nozzle throat diameter d_{n}/mm	14	0.05
	Convergent section arc radius r_{s}/mm	4	0.05
	Burning surface radius r_{b}/mm	120	0.5
Propellant property parameters	Propellant density ρ_{p}/(kg m^{-3})	1700	5
	Burn rate r/(mm s^{-1})	15	0.1
	Characteristic velocity c^*/(m s^{-1})	1400	5
	Pressure exponent n	0.30	0.005

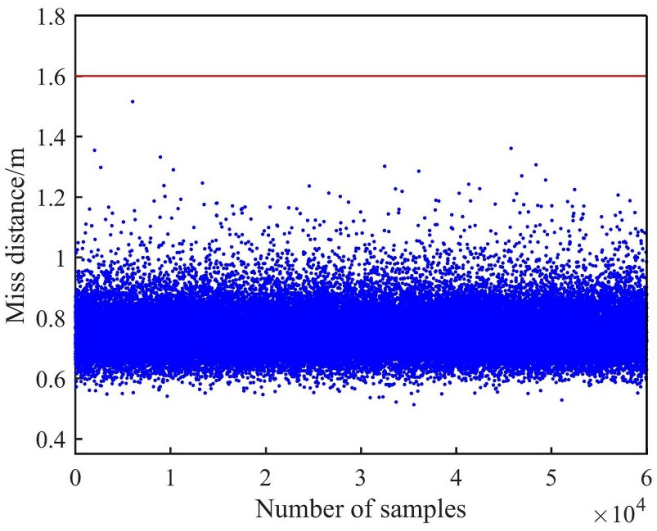


Figure 7. MCS dispersion of miss distance.

As shown in table 3, a total of 10 random variables are considered; therefore, a 10-dimensional PCE surrogate model is constructed in this study. For high-dimensional PCE models, an appropriate hyperbolic truncation parameter q can effectively reduce computational cost while maintaining model accuracy. In this work, q is set to 0.9. Let N denote the number of sample points. To ensure the invertibility of the regression matrix, the sampling size must satisfy $N \geqslant Q+1$. According to the literature, it is recommended that the number of sample points be at least twice the number of unknown PCE coefficients.

Accordingly, the integrated internal-external ballistic dynamic model of the SDCM can be expressed as follows

$$R_{\mathrm{m}} = g(\mathbf{X}). \tag{19}$$

The input X is a vector composed of 10 random variables, and the output R_{m} denotes the miss distance of the kinetic interceptor. The true response model $g(\mathbf{X})$ is evaluated at the sample points, and the corresponding response values are obtained as $\mathbf{G} = [g(\mathbf{X}_1), g(\mathbf{X}_2) \cdots g(\mathbf{X}_{\mathrm{N}})]^{\mathrm{T}}$ Substituting the Hermite orthogonal polynomial basis and the corresponding function response values into equation (17) yields

$$\begin{bmatrix} \Phi_0(\xi_1) & \Phi_1(\xi_1) & \cdots & \Phi_P(\xi_1) \\ \Phi_0(\xi_2) & \Phi_1(\xi_2) & \cdots & \Phi_P(\xi_2) \\ \vdots & \vdots & & \vdots \\ \Phi_0(\xi_N) & \Phi_1(\xi_N) & \cdots & \Phi_P(\xi_N) \end{bmatrix} \begin{bmatrix} b_0 \\ b_0 \\ \vdots \\ b_P \end{bmatrix} = \begin{bmatrix} g(\mathbf{X_1}) \\ g(\mathbf{X_2}) \\ \vdots \\ g(\mathbf{X_N}) \end{bmatrix}. \tag{20}$$

The coefficients of the PCE model can be obtained using the least-squares method, and are expressed as follows

$$\mathbf{b} = (\mathbf{A}^{\mathrm{T}}\mathbf{A})^{-1}\mathbf{A}^{\mathrm{T}}\mathbf{G} \tag{21}$$

where $\mathbf{A} = \begin{bmatrix} \Phi_0(\xi_1) & \Phi_1(\xi_1) & \cdots & \Phi_P(\xi_1) \\ \Phi_0(\xi_2) & \Phi_1(\xi_2) & \cdots & \Phi_P(\xi_2) \\ \vdots & \vdots & & \vdots \\ \Phi_0(\xi_N) & \Phi_1(\xi_N) & \cdots & \Phi_P(\xi_N) \end{bmatrix}$;

$\mathbf{b} = \begin{bmatrix} b_0 \\ b_1 \\ \vdots \\ b_P \end{bmatrix}$.

A total of 3500 sample points were generated over the entire input space using OLHS [30]. The first 3000 samples were used to construct PCE surrogate models with expansion orders of $p = 1 \sim 5$, and the remaining 500 samples were reserved as an independent test set to assess the predictive accuracy of each surrogate model. The predictive accuracy of the surrogate models is evaluated using the coefficient of determination R^2, root mean square error e_{RMSE}, relative average absolute error e_{RAAE}, and relative maximum absolute error e_{RMAE} [31]. Figure 8 shows the variation of the evaluation metrics as a function of the expansion order p.

Among them, the coefficient of determination R^2 is used to evaluate the overall fitting capability of the surrogate model; the closer its value is to 1, the higher the global fitting accuracy. The root mean square error e_{RMSE} and the relative average absolute error e_{RAAE} are employed to assess the global predictive accuracy of the model; the closer their values are to 0 [32], the higher the global prediction accuracy. The relative maximum absolute error e_{RMAE} is used to evaluate the local accuracy of the model; the closer its value is to 0, the higher the local prediction accuracy. The expressions of these four evaluation metrics are given as follows

$$\begin{cases} R^2 = 1 - \sum_{i=1}^{n} (g_i - \hat{g}_i)^2 / \sum_{i=1}^{n} (g_i - \bar{g}_i)^2 \\ e_{\mathrm{RMSE}} = \sqrt{\frac{1}{n}\sum_{i=1}^{n} (g_i - \hat{g}_i)^2} \\ e_{\mathrm{RAAE}} = \sum_{i=1}^{n} |g_i - \hat{g}_i| / (n \cdot \mathrm{mean}(g)) \\ e_{\mathrm{RMAE}} = \frac{\max(|g_i - \hat{g}_i|, \cdots, |g_n - \hat{g}_n|)}{\mathrm{mean}(g)} \end{cases} \tag{22}$$

where n denotes the number of test samples; g_i is the true value of the ith test sample; $\hat{g}_i$ represents the predicted value of the ith test sample; and $\mathrm{mean}(g)$ denotes the average of the true values over all test samples.

As shown in figure 8(a), the coefficient of determination R^2 reaches its maximum and the relative maximum absolute error e_{RMAE} reaches its minimum at $p = 4$, indicating the best overall fitting capability and local prediction accuracy. When the order is further increased to $p = 5$, R^2 decreases slightly while e_{RMAE} increases, suggesting a decline in prediction performance.

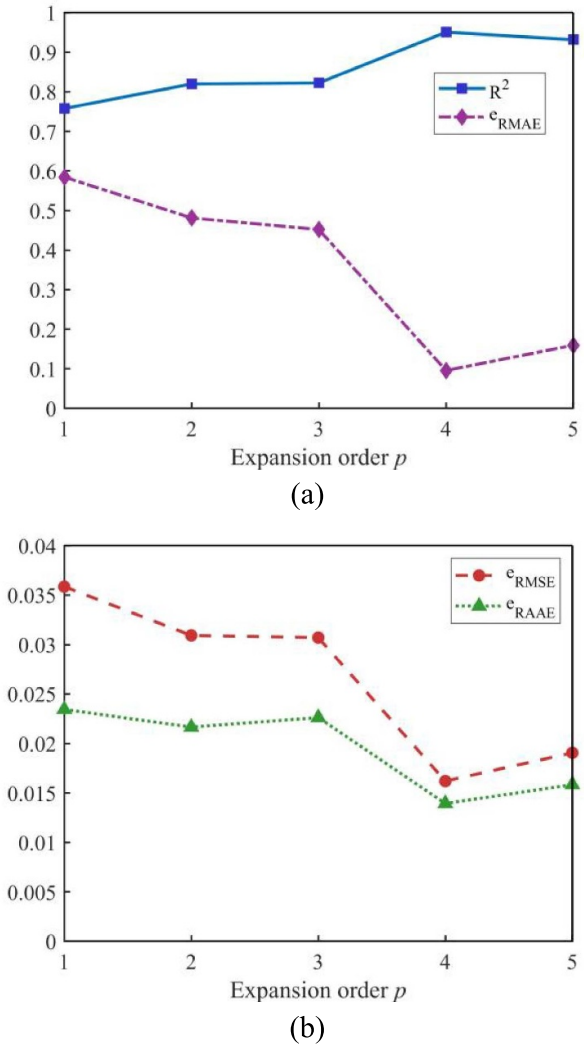


Figure 8. Variations of model evaluation metrics with the expansion order p (a) variations of R^2 and e_{RMAE} with the expansion order p, and (b) variations of e_{RMSE} and e_{RAAE} with the expansion order p.

Table 4. The four evaluation metrics of the PCE ($p = 4$) and Kriging surrogate models for the test samples.

Model	R^2	e_{RMSE}	e_{RAAE}	e_{RMAE}
PCE	0.951	0.016	0.014	0.096
Kriging	0.962	0.012	0.021	0.272

As shown in figure 8(b), the error metrics e_{RMSE} and e_{RAAE}, generally decrease with increasing expansion order and reach their minimum values at $p = 4$, followed by a certain degree of increase at $p = 5$. Based on the variation trends of all evaluation metrics, it can be concluded that the surrogate model achieves optimal predictive accuracy at $p = 4$.

Table 4 presents the evaluation metrics calculated from the prediction results of the 500 test samples obtained by the fourth-order PCE and Kriging surrogate models.

Table 4 compares the prediction performance of the PCE and Kriging surrogate models using 500 independent test samples. The Kriging surrogate model yields a slightly higher R^2

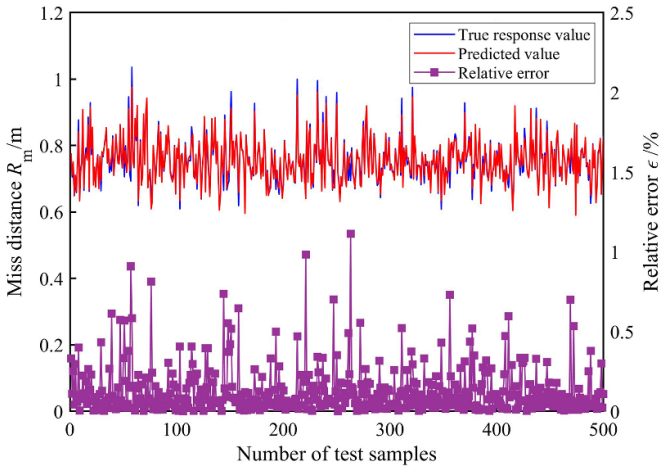


Figure 9. The true response values, predicted values and relative errors of 500 groups of samples.

and a lower e_{RMSE}, whereas the PCE surrogate model exhibits lower e_{RAAE} and e_{RMAE} values, indicating better average relative prediction accuracy. Both surrogate models achieve high prediction accuracy, demonstrating their capability to approximate the integrated internal-external ballistic model.

Although the Kriging surrogate model exhibits comparable predictive performance, PCE is more suitable for the uncertainty quantification framework considered in this study. PCE provides an explicit analytical representation of the system response, facilitates the computation of statistical moments, and enables the direct calculation of both first-order and total-effect Sobol indices without additional sampling. In contrast, the calculation of Sobol indices based on Kriging models generally requires additional sampling procedures or numerical integration, resulting in increased computational costs and potential additional uncertainties. Therefore, the fourth-order PCE surrogate model is adopted for subsequent uncertainty propagation and sensitivity analyses.

Figure 9 presents the prediction results and relative errors of the fourth-order PCE surrogate model for the 500 test samples.

The relative errors of all test samples remain below 1.5%, indicating that the fourth-order PCE possesses high local accuracy. Therefore, the surrogate model can accurately characterize the system response and is suitable for subsequent uncertainty analysis.

3.2. *Uncertainty analysis of miss distance*

Based on the constructed PCE surrogate model, MCS is further employed to perform uncertainty analysis of the miss distance. Table 5 lists the first four statistical moments of the miss distance obtained from the integrated internal-external ballistic dynamic model and predicted by the PCE surrogate model.

The deviations in the mean and standard deviation of the miss distance obtained by the two methods are relatively small, indicating that the PCE surrogate model achieves high accuracy in predicting the miss distance for uncertainty analysis.

Table 5. The first four statistical moments of miss distance.

R_m	Mean	Standard deviation	Skewness	Kurtosis
MCS	0.7541	0.0697	1.0652	6.8240
PCE-MCS	0.7542	0.0687	0.8051	6.6747

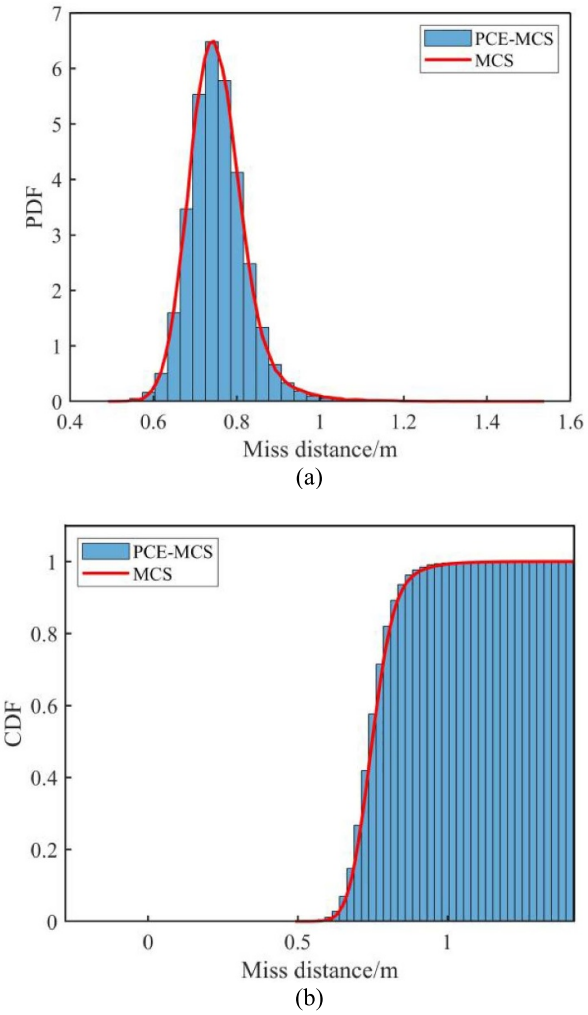


Figure 10. (a) PDF curve of miss distance and (b) CDF curve of miss distance.

Figure 10 presents the probability density function (PDF) and cumulative distribution function (CDF) curves of the miss distance.

As shown in figure 10, the probability density estimated by the PCE surrogate model agrees well with both the histogram of the predicted samples and the MCS-based probability curve. The miss distance is primarily distributed within the range of 0.4–1.6 m, and its PDF exhibits a right-skewed distribution. In terms of computational efficiency, the proposed PCE surrogate model exhibits a significant advantage. A single evaluation of the integrated internal-external ballistic dynamic model requires approximately 9.8 s, whereas a single prediction using the PCE surrogate model requires only 6.6 ms, resulting in a substantial reduction in computational cost.

3.3. PCE-based Sobol' sensitivity analysis

Sobol sensitivity analysis is widely used for nonlinear and non-monotonic models because it enables the efficient computation of first-order, higher-order, and total-order sensitivity indices for input parameters [33]. Among various global sensitivity analysis methods, the Sobol indices are one of the most widely used sensitivity measures. The Sobol method is based on variance decomposition, in which the total variance of the model response is decomposed into the contributions of individual input variables and their interaction effects [34, 35]. Accordingly, let $g(X)$ denote the response function of the input vector $X=(x_1,\cdots,x_d)$, which can be decomposed as follows

$$g(X)=g_0+\sum_{s=1}^{d}\sum_{i_1<\cdots i_s}^{d} g_{i_1\cdots i_s}(x_{i_1},\cdots,x_{i_s}) \tag{23}$$

where $1\leqslant i_1<\cdots<i_s\leqslant d$.

Further decomposition of equation (23) yields

$$\begin{aligned} g(X)&=g_0+\sum_{i=1}^{d} g_i(x_i)\\ &+\sum_{1\leqslant i<j\leqslant d}^{d} g_{i,j}(x_i,x_j)+\cdots+g_{1,2\cdots,d}(x_1,x_2,\cdots,x_d) \end{aligned} \tag{24}$$

where g_0 denotes the constant term; x_i represents the ith input variable; $g(x_i)$ denotes the function involving only the individual effect of x_i; and $g_{i,j}(x_i,x_j)$ represents the function describing the interaction effect between x_i and x_j. The higher-order terms can be defined analogously.

When the following orthogonality condition is satisfied $\int_0^1 g_{i_1\cdots i_s}(x_{i_1},\cdots,x_{i_s})\mathrm{d}x_k=0, k=i_1,\cdots,i_s$, the decomposition in equation (24) is unique, and all component terms are mutually orthogonal. By integrating equation (24), the first-order and second-order variance components can be obtained, as shown in equations (25)–(27)

$$\int g(X)\,\mathrm{d}x=g_0 \tag{25}$$

$$\int g(X)\prod_{k\neq i}\mathrm{d}x_k=g_0+g_i(x_i) \tag{26}$$

$$\int g(X)\prod_{k\neq i,j}\mathrm{d}x_k=g_0+g_i(x_i)+g_j(x_j)+g_{i,j}(x_i,x_j). \tag{27}$$

The remaining component terms can be obtained analogously. According to the definition of variance for continuous variables, squaring both sides of equation (23) and integrating over the input space yields

$$\int g^2(X)\,\mathrm{d}x-g_0^2=\sum_{s=1}^{d}\sum_{i_1<\cdots<i_s}^{d}\int g^2_{i_1\cdots i_s}(x_{i_1},\cdots,x_{i_s})\,\mathrm{d}x_{i_1}\cdots\mathrm{d}x_{i_s} \tag{28}$$

where $\int g^2(X)\mathrm{d}x-g_0^2$ represents the total variance D of the output response; and $\int g^2_{i_1\cdots i_s}(x_{i_1},\cdots,x_{i_s})\mathrm{d}x_{i_1}\cdots\mathrm{d}x_{i_s}$ denotes the variance contribution $D_{i_1\cdots i_s}$ of the input variables $x_{i_1}\cdots x_{i_s}$ to the output response.

Therefore, equation (28) can be expressed as follows

$$\begin{aligned} D&=\int g^2(X)\,\mathrm{d}x-g_0^2\\ &=\sum_{s=1}^{n}\sum_{i_1<\cdots<i_s}^{n}\int g^2_{i_1\cdots i_s}(x_{i_1},\cdots,x_{i_s})\,dx_{i_1}\cdots dx_{i_s}\\ &=\sum_{s=1}^{n}\sum_{i_1<\cdots<i_s}^{n} D_{i_1\cdots i_s}. \end{aligned} \tag{29}$$

The variance-based sensitivity index is defined as the ratio of the variance contribution associated with an input variable to the total variance of the output response. Therefore, by dividing both sides of equation (29) by the total variance D and performing further decomposition, the following expression can be obtained

$$1=\sum_{i=1}^{d}S_i+\sum_{1\leqslant i<j\leqslant d}^{d}S_{ij}+\cdots+S_{1,2,\cdots,d}. \tag{30}$$

Therefore, the first-order sensitivity index S_i can be expressed as

$$S_i=\frac{D_i}{D}. \tag{31}$$

For the input variable x_i, the total sensitivity index S_i^{T} is defined as the sum of all Sobol indices involving x_i, which can be expressed as

$$S_i^{\mathrm{T}}=1-\frac{D_{\sim i}}{D} \tag{32}$$

where $D_{\sim i}$ represents the conditional variance contribution of all input variables except x_i to the output response.

The first-order sensitivity index S_i reflects the influence of an individual parameter x_i on the miss distance of the kinetic interceptor, while the total sensitivity index S_i^{T} represents the overall influence of x_i, including its interaction effects with all other input parameters, on the miss distance. A larger difference between S_i^{T} and S_i indicates stronger interactions between x_i and the other parameters.

The Sobol sensitivity indices can be efficiently and accurately obtained based on the PCE model [36]. In this study, the PCE surrogate model constructed according to section 3.1 is employed to calculate the first-order sensitivity indices S_i and total sensitivity indices S_i^{T}, and the results are presented in table 6.

The analysis of the first-order sensitivity indices indicates that the burning surface radius, pintle diameter, nozzle throat diameter, and burning rate are the dominant factors affecting the uncertainty of the miss distance, with first-order sensitivity indices of 0.209, 0.208, 0.178, and 0.123, respectively. These

Table 6. Sensitivity analysis results of the miss distance with respect to each random variable.

Random variable		First-order sensitivity indices	Total-order sensitivity indices
Control deviation	Pintle displacement Δx_h	0.035	0.165
Geometric parameters	Pintle diameter d_h	0.208	0.269
	Pintle head length L_t	0.010	0.023
	Nozzle throat diameter d_n	0.178	0.248
	Convergent section arc radius r_s	0.006	0.010
	Burning surface radius r_b	0.209	0.212
Propellant property parameters	Propellant density ρ_p	0.025	0.027
	Burn rate r	0.123	0.127
	Characteristic velocity c^*	0.039	0.040
	Pressure exponent n	0.023	0.025

parameters account for the majority of the output variance contribution. Among them, the burning surface radius exhibits the highest first-order sensitivity index, indicating that deviations in propellant geometric parameters have a significant influence on the performance dispersion of the system. The burning surface radius directly determines the propellant burning area, and its deviation affects the evolution of chamber pressure and the thrust output characteristics of the motor. The uncertainty in burning surface radius propagates through the pressure variation-thrust response-flight trajectory chain and ultimately affects the miss distance.

For the nozzle geometric parameters, the first-order sensitivity indices of the pintle diameter and nozzle throat diameter are 0.208 and 0.178, respectively. These two parameters jointly determine the effective throat area of the nozzle, which directly affects the propellant mass flow rate and chamber pressure level. Deviations in critical nozzle dimensions alter the thrust regulation characteristics of the motor and further influence the control performance during the external ballistic phase. In contrast, the first-order sensitivity indices of the pintle head length and convergent section arc radius are only 0.010 and 0.006, respectively, indicating that their direct effects on the effective flow area and thrust output are relatively limited, resulting in minor contributions to the variance of the miss distance.

Figure 11 provides a more intuitive comparison of the influence of each random variable on the uncertainty of the integrated internal-external ballistic performance of the SDCM.

As shown in figure 11, further comparison between the first-order sensitivity index S_i and the total sensitivity index S_i^T reveals that the total sensitivity indices of all uncertain variables are higher than their corresponding first-order sensitivity indices, indicating that the interaction effects among variables cannot be neglected. Among all uncertain variables, the difference between S_i and S_i^T for the pintle displacement deviation is the largest, demonstrating a strong interaction effect. This is because the pintle motion directly determines the variation of the effective nozzle throat area. Its influence depends not only on its own motion deviation but also on the coupled effects of

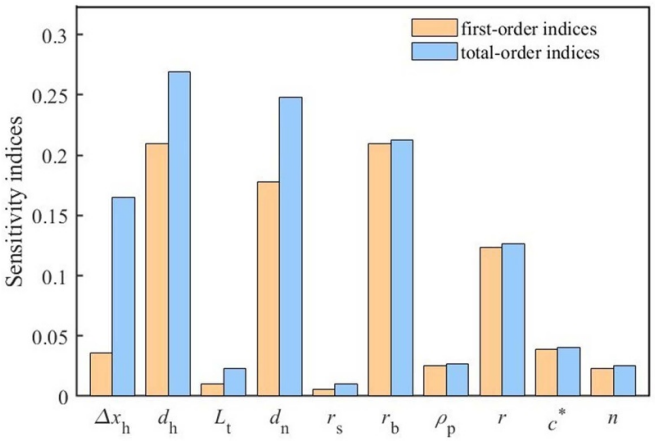


Figure 11. Sensitivity indices of the miss distance with respect to different random variables.

pintle parameters, nozzle geometric parameters, and propellant combustion characteristics, resulting in multi-parameter interaction and uncertainty propagation.

In addition, relatively large differences between the first-order and total sensitivity indices are also observed for the pintle diameter and nozzle throat diameter, indicating significant interaction effects associated with these two geometric parameters during motor operation. Considering the coupling effects among different parameters, the global importance ranking of uncertain variables affecting the uncertainty of the integrated internal-external ballistic performance of the SDCM is obtained as follows: pintle diameter > nozzle throat diameter > burning surface radius > pintle displacement deviation > burn rate > characteristic velocity > propellant density > pressure exponent > pintle head length > convergent section arc radius.

The integrated internal-external ballistic performance of the SDCM is highly sensitive to key geometric parameters, including the pintle diameter, nozzle throat diameter, and

burning surface radius, as well as the pintle displacement deviation. To effectively reduce the dispersion of the miss distance and improve the strike accuracy of kinetic interceptors, strict control of the machining tolerances of the pintle diameter and nozzle throat diameter, together with high-precision fabrication of the propellant burning surface, should be emphasized during the design and manufacturing stages of the motor. Considering the strong coupling effects between the pintle displacement deviation and structural parameters, future optimization design of SDCMs should evolve from single-parameter accuracy control toward multi-parameter collaborative optimization. This approach can reduce the propagation of uncertainties in the coupled internal-external ballistic system and further improve the terminal strike accuracy of kinetic interceptors.

4. Conclusions

In this study, an integrated internal-external ballistic dynamic model of a SDCM is established by considering multiple sources of uncertainty, including pintle displacement deviation, geometric deviation, and propellant property uncertainties. Based on this integrated model, MCS and a PCE surrogate model are employed to investigate the effects of multi-source uncertainties on the integrated internal-external ballistic performance. The main findings are summarized as follows:

(1) A performance dispersion analysis method for the integrated internal-external ballistics of SDCMs is proposed. Compared with traditional deterministic evaluation methods that separately analyze internal and external ballistics, the proposed method enables rapid prediction of integrated internal-external ballistic performance dispersion by considering the propagation of multi-source uncertainties, while maintaining high predictive accuracy. It provides an effective approach for uncertainty analysis of the integrated internal-external ballistic system of SDCMs.
(2) The results demonstrate that the proposed PCE-based uncertainty analysis method achieves high predictive accuracy. The miss distance exhibits a right-skewed distribution and is mainly concentrated within the range of 0.4–1.6 m, indicating that the coupled effects of multi-source uncertainties are more likely to increase the miss distance.
(3) The Sobol' sensitivity analysis method was employed to quantitatively characterize the individual and interaction contributions of each uncertain parameter to the variance of the miss distance. The pintle diameter, nozzle throat diameter, and burning surface radius exhibit relatively high first-order and total sensitivity indices, indicating that they are the dominant factors affecting the dispersion of the miss distance. Although the pintle displacement deviation has a relatively low first-order sensitivity index, it exhibits strong coupling interactions with other structural parameters. These results reveal the influence mechanisms of different uncertain variables on the performance dispersion of the integrated internal-external ballistic system of SDCMs, and provide theoretical support for key parameter tolerance allocation, manufacturing accuracy control, and robust optimization design for high-precision control.

Although the proposed framework has demonstrated good effectiveness, several limitations still remain. Firstly, all geometric and propellant property parameters are assumed to follow normal distributions in the present study. However, in practical manufacturing processes and service environments, some geometric tolerances or random errors may exhibit arbitrary non-normal distributions. Secondly, to balance computational efficiency during large-scale sampling, the internal ballistic module in this study is primarily solved based on zero-dimensional internal ballistic differential equations. This simplified physical model does not fully capture complex phenomena occurring during the short-duration divert maneuver of the motor, such as thrust misalignment and dynamic ablation of the nozzle pintle caused by high-temperature combustion gases. Addressing these aspects will be the focus of subsequent studies.

Acknowledgment

This work was supported by National Natural Science Foundation of China (Grant No. 52375278), the Science and Technology Innovation Program of Hunan Province (Grant No. 2024RC3142).

ORCID iD

Li Shuaiwei 0009-0007-1534-9036

References

[1] Yang X-M, Ren Q-B and Ai C-A 2022 Progress on gas valve technology of solid KKV divert and attitude control system *J. Solid Rocket Technol.* **45** 902–7
[2] Ma S, Guo J-X, Zhou L and Zhu Z-H 2023 Review on technology development of solid rocket motor *J. Rocket Propul.* **49** 1–14
[3] dos Santos P and Oliveira P 2024 Integrated architecture for navigation and attitude control of low-cost suborbital launch vehicles *Acta Astronaut.* **222** 52–68
[4] Zhang D-Q, Zhao Y, Yang M-D, Jiang C, Han X and Li Q 2025 Time series clustering adaptive enhanced method for time-dependent reliability analysis and design optimization *Comput. Methods Appl. Mech. Eng.* **443** 118099
[5] Ponti F, Mini S, Fadigati L, Ravaglioli V, Annovazzi A and Garreffa V 2021 Effects of inclusions on the performance of a solid rocket motor *Acta Astronaut.* **189** 283–97
[6] Golpashin A E, Yeong H C, Ho K and Namachchivaya N S 2020 Spacecraft attitude control: a consideration of thrust uncertainty *J. Guid. Control Dyn.* **43** 2349–65
[7] Zhang J, Li G-S, Wen Q, Wang D-H, Wu Z-P and Zhang W-H 2023 Fast thrust prediction method for solid divert and attitude control system based on improved augmented radial basis functions *J. Propul. Technol.* **44** 206–14

[8] Lei J-C, Yang Y, Xu W-L, Ma M-Y and Song H 2022 Research on the integrated design method of internal and external ballistics of solid rocket *Missiles Space Veh.* pp 13–17
[9] Wu W-X, Shao C-X, Zhu M-C and Zhang X-Q 2025 Integrated optimization design of internal and external ballistics for low-altitude cruise target missiles *J. Projectiles, Rockets, Missiles Guidance* **45** 1202–10
[10] Su W-X, Dai L, Zhang F and Yu J-Y 2023 Joint optimization for solid rocket motor based on the system optimal strategy *Missiles Space Veh.* pp 7–10
[11] Zhang D-Q, Li W-R, Zhang H-F, Wang D-P, Wu Z-P and Niu L 2026 Uncertainty modeling and thrust quantitative analysis for servomechanism of solid divert control motor *J. Astronaut.* **47** 883–94
[12] Gao J-W, Jia J-K, Wu Z-P, Zhang D-Q, Zhang J and Zhang W-H 2025 Uncertainty analysis of thrust during variable operating condition process of solid divert and attitude control motor *J. Natl Univ. Def. Technol.* **47** 94–104
[13] Zhu H, Xiao M-Y, Zhang J-H and Cai G-B 2022 Uncertainty design and optimization of a hybrid rocket motor with mixed random-interval uncertainties *Aerosp. Sci. Technol.* **128** 1–12
[14] Xiao M-Y, Zhu P-P, Zhu H and Cai G-B 2025 Uncertainty quantification of hybrid rocket motor mass based on evidence theory *Astronaut. Syst. Eng. Technol.* **9** 64–70
[15] Shi M-Y, Li C-N, Liu Y and Gong C-L 2025 Accurate surrogate modeling method for solid rocket motor performance under uncertainty *J. Propul. Technol.* **46** 37–46
[16] Balesdent M, Brevault L, Valderrama-zapata J-L and Urbano A 2022 All-at-once formulation integrating pseudo-spectral optimal control for launch vehicle design and uncertainty quantification *Acta Astronaut.* **200** 462–77
[17] Wen Q, Yang J-W, Wu Z-P, Yang X-Y, Peng B and Zhang W-H 2022 Time-sequence experiment design for pintle motion scheme of solid divert and attitude control system *J. Propul. Technol.* **43** 354–63
[18] Tang J-L and Liu P-J 2013 *Principle of Solid Rocket Motor* (National Defense Industry Press) pp 263–93
[19] Wang D, Feng F and Chen J 2016 *Fundamentals of Solid Rocket Motor* (Institute of Technology Press) pp 232–57
[20] Yan D-F, Wei Z-J, Xie K and Wang N-F 2020 Simulation of thrust control by fluidic injection and pintle in a solid rocket motor *Aerosp. Sci. Technol.* **99** 105711
[21] Jia J-K, Zhang D-Q, Zhang H-F, Wu Z-P, Zhang J and Xie Z-Y 2025 Static and dynamic uncertainty analyses for thrust regulation performance of solid divert and attitude control motor *Acta Astronaut.* **236** 1257–71
[22] Miao Q, Shen Z, Zhang H and Sun H 2022 Multiobjective optimization method of solid rocket motor finocyl grain based on surrogate model *Aerospace* **9** 679
[23] Zhu M, Li Y-K, Chen X, Mi J-J, Li W-X and Xue H-F 2024 Design of nonlinear control method for pressure of pintle solid rocket motor *Acta Astronaut.* **215** 296–307
[24] Chen K-J, Liu L-H and Meng Y-H 2014 *Long-Range Rocket Flight Dynamics and Guidance* (National Defense Industry Press) pp 66–88
[25] Guo J-G, Han T, Zhou J and Wang G-Q 2017 Terminal guidance law for exoatmospheric kill vehicle with energy optimization method *Syst. Eng. Electron.* **39** 376–82
[26] Zhou D 2002 *New Guidance Laws for Homing Missiles* (National Defense Industry Press) pp 5–20
[27] Li G-S, Ma S-C, Zhang D-Q, Yang L-P, Zhang W-H and Wu Z-P 2024 An efficient sequential anisotropic RBF reliability analysis method with fast cross-validation and parallelizability *Reliab. Eng. Syst. Saf.* **241** 109600
[28] Xiong F-F 2015 *Engineering Probabilistic Uncertainty Analysis Method* (Science Press) pp 1–5
[29] Liu J-X, Yang G-L, Wang L-Q and Xue L-G 2025 Interval uncertainty analysis of ultra-light gun launching process based on polynomial chaos expansion *J. Vib. Shock* **44** 132–9
[30] Wu Z-P, Wang Z-X and Zhang W-H 2023 *Data-driven Metamodeling Methods and Applications* (National Defense Industry Press) pp 31–54
[31] Zhang D-Q, Jia J-K, Wu Z-P, Wang D-H, Niu L and Zhou W-H 2023 Uncertainty analysis on single-valve thrust deviation of pintle solid divert motor *J. Solid Rocket Technol.* **46** 498–506
[32] Parnianifard A, Azfanizam A S, Ariffin M K A and Ismail M I S 2018 An overview on robust design hybrid metamodeling: advanced methodology in process optimization under uncertainty *Int. J. Ind. Eng. Comput.* **1** 1–32
[33] Yin J-Q, Zhao C-C, Chen Y-D, Cheng Y-F and Gu J-Y 2021 Sensitivity of structural parameters of composite reinforced panels based on the Sobol method *Sci. Technol. Eng.* **21** 1735–9
[34] Xu K, Zheng C-J, Yu Z-Q, Sheng Z-F, Zhang G-X, Xiao J-Y and You J-F 2022 Parameter sensitivity analysis of SRM nozzle based on Sobol method *J. Solid Rocket Technol.* **45** 830–7
[35] Zhang J-W, Shao B-H, Chang S-J and Xie F 2022 Global sensitivity analysis of projectile flight motion state *J. Ballist.* **34** 19–27
[36] Ni F, Fan L, Xu J-Q, Lin G-B and Jia W-T 2025 Global sensitivity analysis of single-point levitation system for high-speed maglev train based on Sobol' method *J. Southwest Jiaotong Univ.* **60** 812–22



Shuai-Wei Li is currently a master's student at the College of Aerospace Science and Engineering, National University of Defense Technology. His research focuses on integrated internal-external ballistic modeling of solid divert control motors. He is interested in data-driven metamodeling method, uncertainty propagation, and surrogate model-based overall design optimization of aerospace vehicles.



Ze-Ping Wu is a supervisor at the College of Aerospace Science and Engineering, National University of Defense Technology. His research interests mainly include multidisciplinary optimization and intelligent design methods, digital design platforms and digital mock-ups, cross-medium super cavitation vehicle technologies, and supercritical medium power technologies and equipment. He has developed a series of demonstration software systems for aircraft conceptual design and successfully facilitated the engineering application of related software and theoretical methodologies.



Jun-Kai Jia is a PhD student at the College of Aerospace Science and Engineering, National University of Defense Technology. His research interests mainly focus on the design and uncertainty analysis of solid attitude and divert control motors.



Lei Tian is a PhD student at the College of Aerospace Science and Engineering, National University of Defense Technology. His research interests mainly focus on aircraft conceptual design and transfer optimization.



Tian-Ci Wang is a PhD student at the College of Aerospace Science and Engineering, National University of Defense Technology. His research interests mainly include surrogate modeling and optimization of solid attitude and divert control motors.



Jie Zhang is a PhD student at the College of Aerospace Science and Engineering, National University of Defense Technology. His research interests mainly include the design and optimization of solid attitude and divert control motors.